

Supplementary Information

Stabilizing low symmetry-based functions of materials at room temperature through isosymmetric electronic bistability

Francisco Javier Valverde-Muñoz,¹ Ricardo Guillermo Torres Ramírez,¹ Elzbieta Trzop,^{1,2} Thierry Bataille,³ Nathalie Daro,⁴ Dominique Denux,⁴ Philippe Guionneau,⁴ Hervé Cailleau,¹ Guillaume Chastanet,⁴ Boris Le Guennic,³ Eric Collet^{1,2,5*}

¹ Univ Rennes, CNRS, IPR (Institut de Physique de Rennes) - UMR 6251, 35000 Rennes, France

² CNRS, Univ Rennes, DYNACOM (Dynamical Control of Materials Laboratory) - IRL 2015, The University of Tokyo, 7-3-1 Hongo, Tokyo 113-0033, Japan

³ Univ Rennes, Ecole Nationale Supérieure de Chimie de Rennes, CNRS, ISCR (Institut des Sciences Chimiques de Rennes) - UMR 6226, F-35000 Rennes, France

⁴ Univ. Bordeaux, CNRS, Bordeaux INP, ICMCB, UMR5026, F-33600 Pessac, France

⁵ Institut Universitaire de France (IUF)

Contents

Supplementary Section 1: X-Ray diffraction experimental details.

Supplementary Section 2: Intra-molecular structural reorganization.

Supplementary Section 3: Thermal dependence of lattice parameters and calculations of the volume strain and ferroelastic distortion.

Supplementary Section 4: Symmetry-breaking Bragg peaks.

Supplementary Section 5: DFT calculations.

Supplementary Section 6: Landau model of coupled symmetry-breaking and SCO.

Supplementary Section 7: Differential scanning calorimetry measurements.

Supplementary video 1: Unstable torsion mode Q_T in the $HShs$ state.

Supplementary Section 1: X-Ray diffraction experimental details.

2a. Single-crystal X-Ray diffraction

Single crystals were mounted on cryo-loops with Parabar 10312 oil. Data for structure determination were collected on an Xcalibur 3 four-circle diffractometer (Oxford Diffraction) equipped with a 2D Sapphire3 CCD detector with an enhanced source using Mo K α radiation ($\lambda = 0.71073 \text{ \AA}$). Nitrogen flow 700 series cryostat from Oxford Cryosystems was used for the variable-temperature measurements. Complete datasets were taken respectively at 90 K and 300 K (Table S1). The CrysAlisPRO95 software package from Rigaku Oxford Diffraction was used for all data collections and data processing (indexing, integration, and reduction). All structures were solved by dual direct methods with SHELXT⁶ and refined by full-matrix least-squares on F² using SHELXL⁷ in OLEX^{2,8}. All non-hydrogen atoms were refined anisotropically and H-atoms were constrained by geometry. DFIX restraints have been applied for some aromatic C-C bonds of the PM-PEA ligand in our structural model.

Detailed changes in unit cell volume, cell parameters, and Bragg peaks intensities as a function of temperature were also investigated during cooling from 300 K to 80 K and warming from 80 K to 500 K with 2–3 K steps (200 K.h⁻¹ cooling/heating rate). The duration of the X-ray diffraction measurement for each temperature step was approximately 12 minutes.

In addition, low temperature single crystal X-ray diffraction experiments were performed on this system to confirm the existence of the HSIs phase at 30 K. An Oxford Cryosystems N-Helix open-flow gas cryostat fitted on a SuperNova four-circle diffractometer (Agilent Technologies) with an EoS 2 detector and a Mo micro-source ($\lambda = 0.71073 \text{ \AA}$) was used to rapidly cool a single crystal from 293 to 30 K. The crystal structure of the quenched state was exactly the same as the one reported previously by Guionneau and co-workers.⁸

CCDC 2309697 (90 K) and CCDC 2309698 (300 K) contain the crystal data collection and refinement parameter details for this paper, which can be obtained free of charge via www.ccdc.cam.ac.uk/conts/retrieving.html (or from the Cambridge Crystallographic Data Centre, 12 Union Road, Cambridge CB2 1EZ, U.K.; fax: (+44) 1223-336-033; or deposit@ccdc.ca.ac.uk).

2b. Powder X-Ray diffraction

High temperature powder X-ray diffraction (Fig. S5a) was performed on a Malvern Panalytical Empyrean diffractometer, equipped with a focusing mirror in the Debye-Scherrer geometry, and operating with the CuK $\alpha_{1,2}$ radiation ($\lambda_1 = 1.5406 \text{ \AA}$, $\lambda_2 = 1.5444 \text{ \AA}$). Crystals were gently crushed until a homogeneous powder was obtained. The polycrystalline compound was introduced into a 0.5 mm diameter quartz capillary, and then placed in the centre of an Anton Paar HTK 1200N oven-camera mounted on the goniometer. X-ray powder patterns were collected every 10 K from ambient to 520 K, within a relevant angular range that allowed subsequent Bragg peaks decomposition. Unit cell parameters were determined from Pawley refinement at each temperature up to the phase degradation, using the FullProf suite software.⁹

Table S1. crystallographic data collection and refinement details,

Reference	<i>LSIs</i>	<i>HSIs</i>
Empirical formula	C ₆ H ₈ FeN ₆ S ₂	
Formula weight	736.67	
T (K)	91(5)	300.00(12)
Crystal system	orthorhombic	monoclinic
Space group	Pccn	P2 ₁ /c
a (Å)	14.2537(4)	15.6569(10)
b (Å)	14.2713(5)	14.5792(10)
c (Å)	17.4543(5)	16.8595(9)
α (°)	90	90
β (°)	90	93.153(5)
γ (°)	90	90
V (Å ³)	3550.53(19)	3842.6(4)
Z	4	4
D _c (mg/cm ³)	1.378	1.273
μ (Mo-K _α) (mm ⁻¹)	0.583	0.538
F(000)	1520.0	
Crystal size (mm ³)	0.19 x 0.13 x 0.07	
No. of total reflections	28015	45533
No. of reflections [I>2σ(I)]	3489	7553
R [I>2σ (I)]	0.0425	0.0664
wR [I>2σ (I)]	0.0793	0.0805
S	1.047	1.028

Supplementary Section 2: Intra-molecular structural reorganization.

The structural analysis at the molecular level provides key information on spin crossover and symmetry-breaking. For the first case, the metal-ligand bond lengths are one of the best probes to monitor spin transition. The $\approx 0.2 \text{ \AA}$ variation of the Fe-N bonds is characteristic of a complete HS \leftrightarrow LS conversion in Fe(II)-based SCO materials, as it is a direct response to an important electronic rearrangement, which involves the population – depopulation of the e_g -like molecular orbitals, which have an antibonding character. Table S2 shows the different Fe-N bond length values of the [Fe^{II}(PM-PEA)₂(NCS)₂] coordination compound in the *HSls* and *LShs* phases. In this data it can be seen how the magnitude of the change slightly differs between each coordination bond, with a much more pronounced variation on those where the PM-PEA ligands are involved. The average Fe-N distances in the *HSls* and *LShs* phase are 2.163(2) \AA and 1.958(2) \AA , respectively, which means a bond variation of $\approx 0.2055 \text{ \AA}$ upon the phase transition. This clearly shows a complete interconversion between both spin states, in agreement with magnetic data. Additionally, it is common practice to compare the deviation of the ideal octahedral FeN₆ coordination geometry of the complex in *HS* and *LS* state, by evaluation of the angular ($\Sigma = \sum_{i=1}^{12} |90 - \phi_i|$) and trigonal distortion ($\Theta = \sum_{i=1}^{24} |60 - \theta_i|$), because they are important parameters to rationalize long-live meta-stable states and huge thermal hysteresis.¹ A much more distorted octahedral environment is achieved when the *HSls* phase is generated in [Fe^{II}(PM-PEA)₂(NCS)₂], displaying a significant increase (+95%) of the octahedral trigonal distortion, as shown in Fig. S1 and Table S2.

On the other hand, symmetry-breaking signatures can be identified at the molecular level in [Fe^{II}(PM-PEA)₂(NCS)₂], in relation with the loss of the 2-fold axis that goes through the metal centres along the *c* axis in the *LShs* phase. Table S2 and Fig. S1 show that in the *LShs* phase, due to the presence of the 2-fold axis, there are three pairs of equivalent Fe-N coordination bonds ($Fe-N_1 = Fe-N_1'$, $Fe-N_2 = Fe-N_2'$, $Fe-N_3 = Fe-N_3'$). When this 2-fold axis is lost in the *HSls* phase, the six Fe-N coordination bonds become crystallographically independent. In addition, the relative angles of the two NCS groups (taken Fe-N₁ and Fe-N_{1'} coordination bonds as a reference) with respect to the (*a,c*) plane in the *LShs* phase are also representative of the impact that the symmetry-breaking has over the coordination sphere of the complexes (see Fig. S1). For the *LShs* phase, both NCS groups display identical values for the defined angle (42.99°), while becoming non-equivalent upon the phase transition towards *HSls* phase. Fig. S2 shows that at the supramolecular scale the loss of the C2 axis results in a bending and sliding of the molecular layers lying on the (*a,c*) planes.

	<i>LShs</i> XRD, 90K	<i>HSls</i> XRD, 300K	<i>LShs</i> (DFT)	<i>HSls</i> (DFT)	<i>HSls</i> (DFT)
Fe-N ₁	1.952(2) \AA	2.056(4) \AA	1.9304 \AA	2.0251 \AA	2.0106 \AA
Fe-N _{1'}	1.952(2) \AA	2.052(4) \AA	1.9304 \AA	2.0251 \AA	2.0467 \AA
Fe-N ₂	1.958(2) \AA	2.181(4) \AA	1.9871 \AA	2.2214 \AA	2.2470 \AA
Fe-N _{2'}	1.958(2) \AA	2.168(4) \AA	1.9871 \AA	2.2214 \AA	2.2141 \AA
Fe-N ₃	1.964(2) \AA	2.268(3) \AA	1.9923 \AA	2.3479 \AA	2.3425 \AA
Fe-N _{3'}	1.964(2) \AA	2.252(3) \AA	1.9923 \AA	2.3479 \AA	2.3464 \AA
Fe-N _{av}	1.958(2) \AA	2.163(2) \AA	1.9699 \AA	2.1981 \AA	2.2012 \AA
Σ	58.0(5)	83.3(4)	44.49	90.86	94.83
Θ	89.6(7)	175.5(11)	102.31	205.10	215.22
Fe-N ₁ -S ₁ (°)	162.3(2)	167.0(2)	159.0	155.4	157.7
Fe-N _{1'} -S _{1'} (°)	162.3(2)	163.1(2)	159.0	155.4	152.6

Table S2 Distortion of the FeN₆ octahedron. Metal-ligand bond lengths (\AA) and angles (°) measured by XRD and obtained from DFT (including also the *HSls* state) for [Fe^{II}(PM-PEA)₂(NCS)₂].

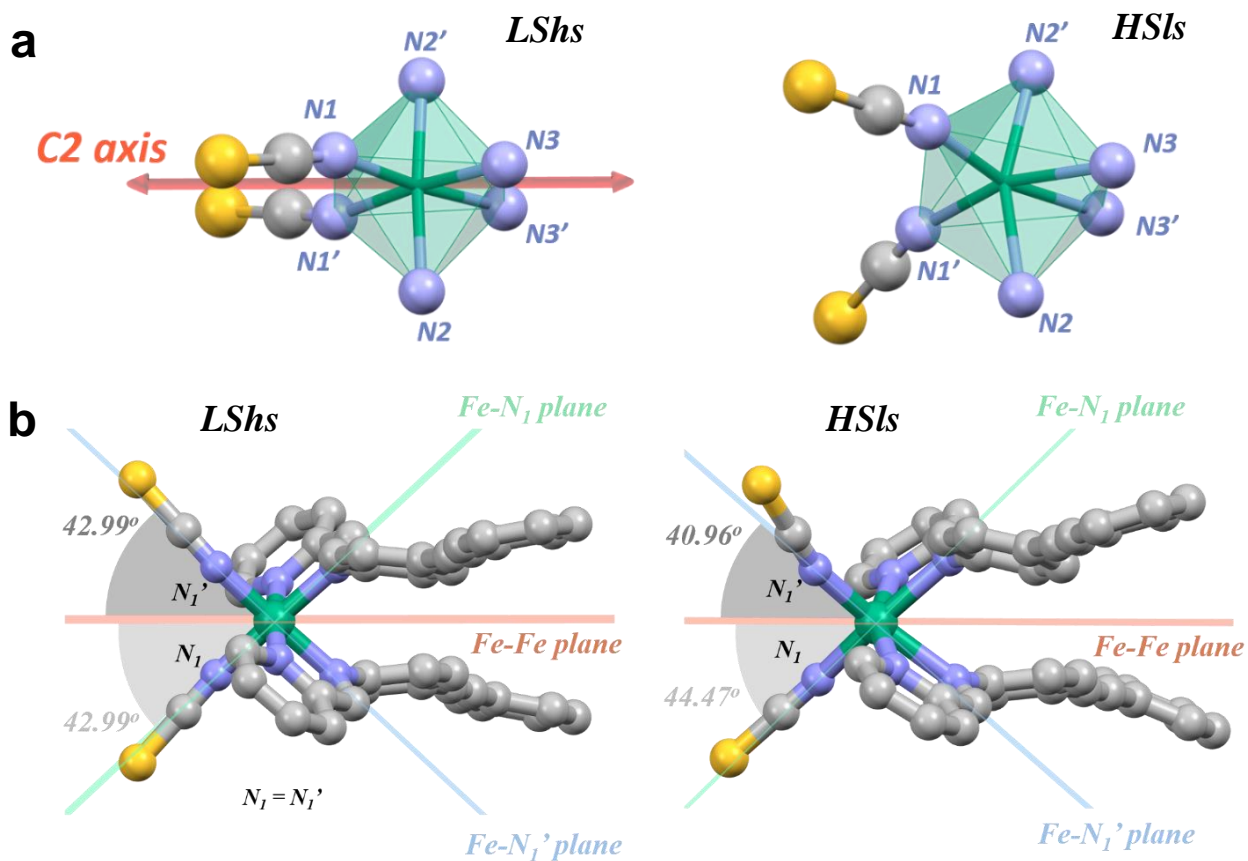


Fig. S1 Molecular deformation upon SCO and SB. **a**, Octahedral coordination sphere around the Fe (green) of $[\text{Fe}^{\text{II}}(\text{PM-PEA})_2(\text{NCS})_2]$ in the *LS* and *HS* phases, where the 2-fold axis is highlighted. **b**, Angular deviation of thiocyanate functional groups with respect to the (a,c) plane which contains the Fe(II) metallic centres.

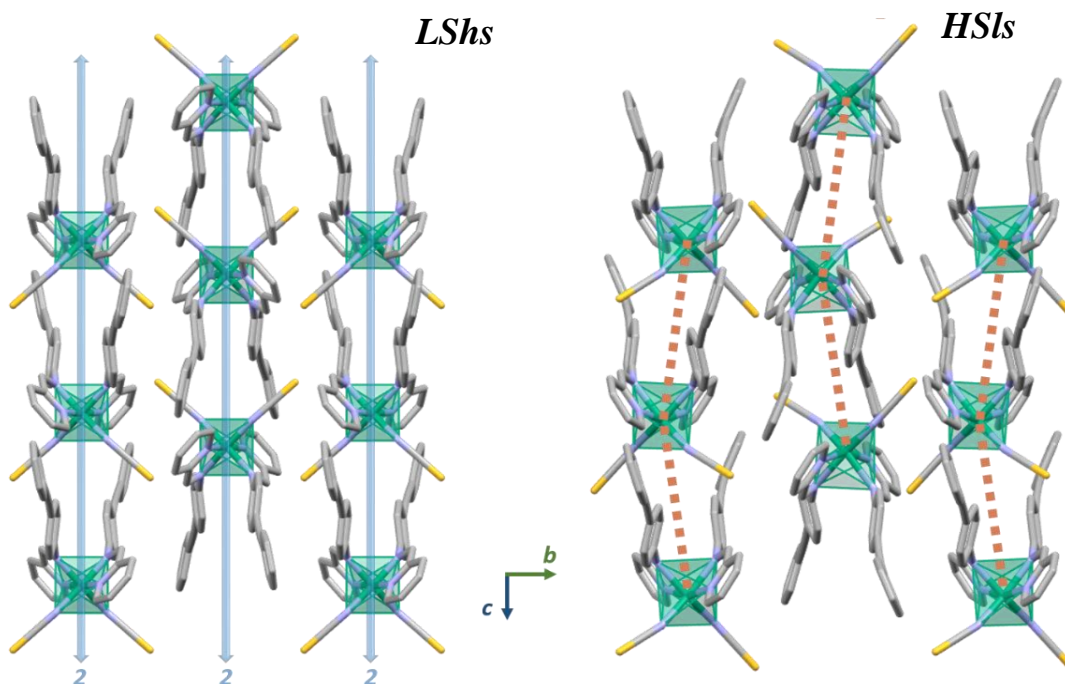


Fig. S2 Molecular deformation within the lattice. With the loss of the C2 axis in the *HS* phase the molecules shift and bend.

Supplementary Section 3: Thermal dependence of lattice parameters and calculations of the volume strain and ferroelastic distortion.

Fig. S3 shows the thermal dependence of the lattice parameters between the *LShs* and *HShs* phases. As reviewed by Carpenter,² ferroelastic phase transitions are characterized by the thermal dependence of:

- the volume strain $v_s(T) = \frac{V(T)}{V_{hs}(T)} - 1$, where $V(T)$ is the measured volume and $V_{hs}(T)$ the volume of the high symmetry phase extrapolated at T in the low symmetry phase (Fig. S3).
- the ferroelastic strain, which corresponds to the $\varepsilon_{13}(T)$ component of the strain tensor²⁻⁴ for the orthorhombic \rightleftharpoons monoclinic ferroelastic distortion; with $\varepsilon_{13}(T) = \frac{1}{2} \left(\frac{c(T) \cos(\beta(T))}{c_{hs}(T)} \right)$, where $c(T)$ and $\beta(T)$ are the measured lattice parameter and $c_{hs}(T)$ the value in the high symmetry phase extrapolated at T in the low symmetry phase (Fig. S3).

The components of the strain tensor are shown in Fig. S4. The partial spin conversion in the *LShs* phase on approaching the phase transition is responsible for the pre-translational volume strain observed in Fig. S3.

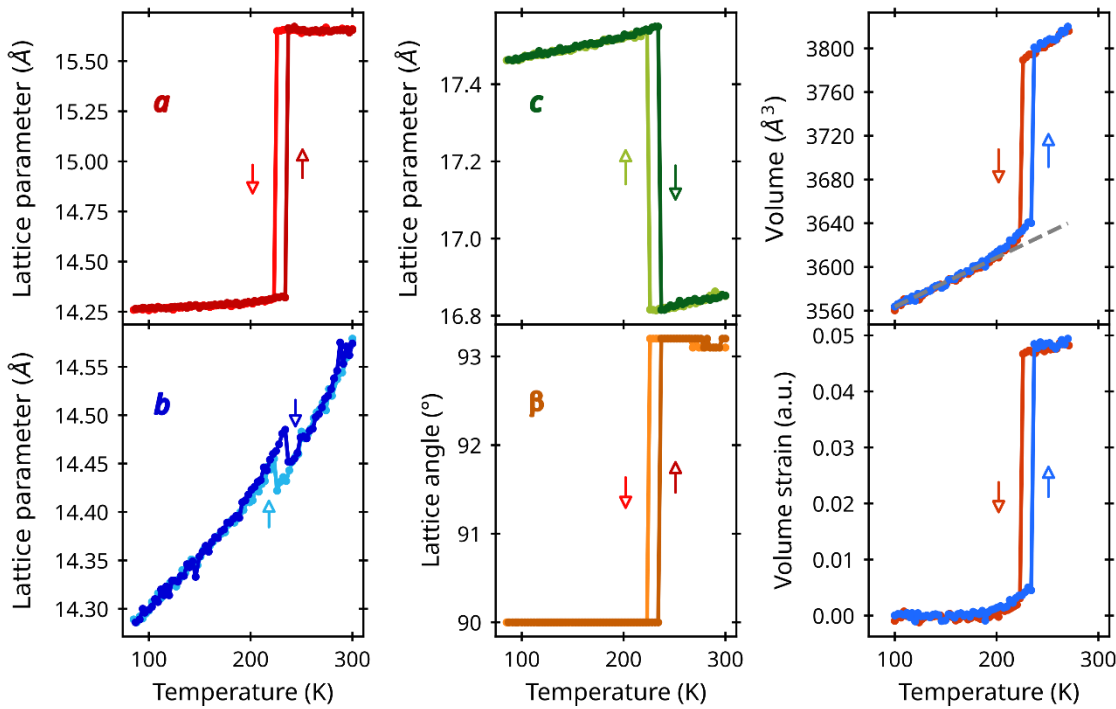


Fig. S3 Thermal dependence of the lattice parameters. The lattice parameters are given in the same unit cell in the *HShs* and *LShs* phases. The volume strain is calculated from the *LShs* phase. The discontinuous changes occur at 218 K on cooling and 238 K on warming.

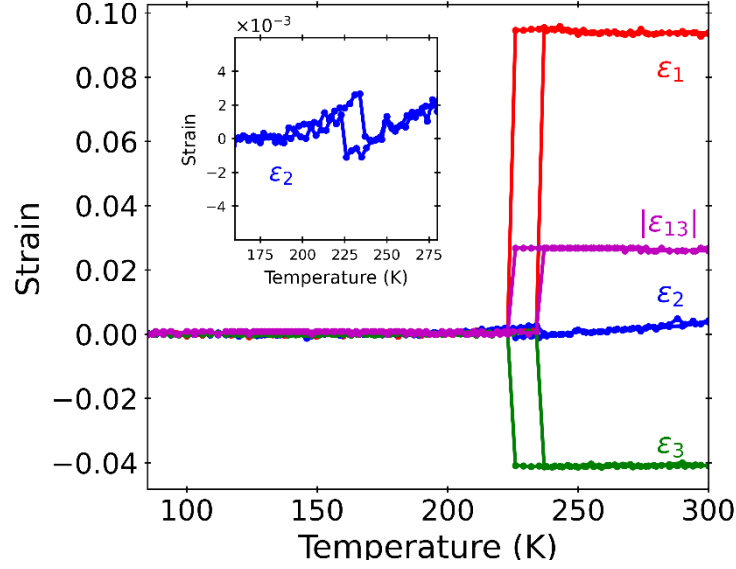


Fig. S4 Thermal dependence of the deformation tensor components. These tensor deformation elements were calculated from Fig. S3, considering the *LShs* phase as a reference and interpolating the thermal dependence in the *HSls* phase. The deformation is weak along the monoclinic crystalline axis (ϵ_2) and highly anisotropic in the (a,c) plane as ϵ_1 increases and ϵ_3 decreases in the *HSls* phase.

The *HSls* phase is characterized by the deviation of the monoclinic β angle from 90° , which results in a splitting of the (hkl) and $(\bar{h}kl)$ Bragg peaks in powder diffraction data (Fig. S5b). The symmetry-breaking order parameter η decreases above 300 K (Fig. S5c), toward a hypothetical *HS* high symmetry phase at ~ 800 K, according to a square root fitting performed on the experimental data (blue dashed line). The *HSls* phase is stable up to $\simeq 500$ K, where melting starts.

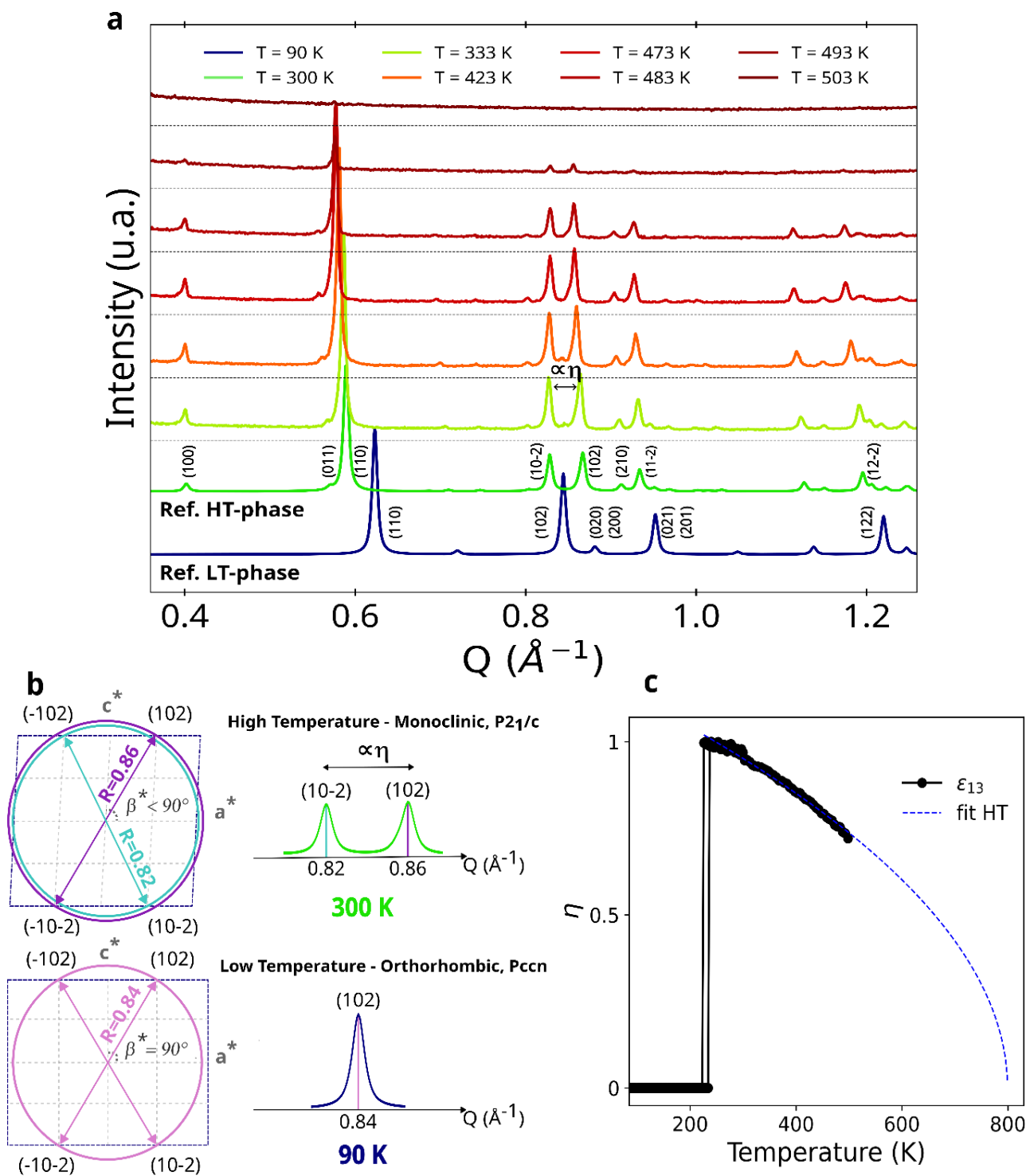


Fig. S5 High temperature low symmetry phase. **a**, X-ray powder diffraction data $I(Q)$ at high temperature, where monoclinic phase transition is characterized by a splitting of the (hkl) and $(\bar{h}kl)$ Bragg peaks due to the ferroelastic strain $\epsilon_{13} \propto \eta$. **b**, the modulus of the reciprocal vectors $|\vec{Q}(10\bar{2})|$ and $|\vec{Q}(102)|$ differ for $\beta \neq 90^\circ$, which translates in a splitting of the $(10\bar{2})$ and (102) Bragg peaks. **c**, decrease of η above 300 K. The *HSLs* phase is stable up to ≈ 500 K, above which the material starts to melt and the diffraction signal is lost.

In a previous crystallography study,⁵ the X-ray diffraction data clearly show that the flash-cooled state corresponds to the monoclinic $P2_1/c$ *HSls* phase (CCDC-632777), with the lattice parameters $a = 15.681(1) \text{ \AA}$, $b = 14.192(1) \text{ \AA}$, $c = 16.634(2) \text{ \AA}$, $\beta = 93.18(1)^\circ$, $V = 3696(1) \text{ \AA}^3$. The crystal packing is identical to the one of the *HSls* phase stable at high temperature, and the Fe(II) coordination sphere geometry clearly indicates that the molecules are in the *HSls* state. On warming, the trapped *HSls* state relax towards the *LShs* orthorhombic phase characterized by the lattice parameters $a = 14.293(1) \text{ \AA}$, $b = 14.304(1) \text{ \AA}$, $c = 17.509(2) \text{ \AA}$, $\beta = 90^\circ$, $V = 3580(1) \text{ \AA}^3$. This thermal relaxation is also characterized by the thermal evolution of the volume strain $v_s(T)$ and the ferroelastic strain $\epsilon_{13}(T)$ shown in Fig. S6, which confirms that the *LShs* phase corresponds to the ground state.

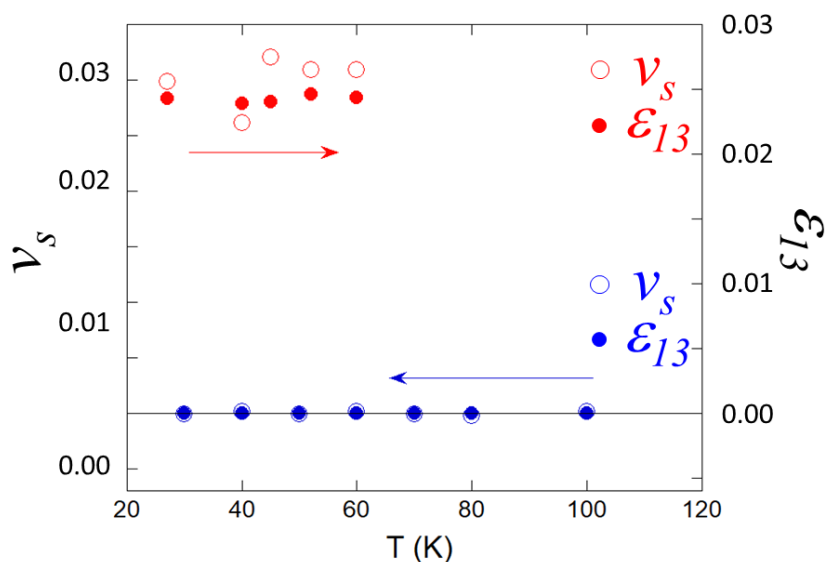


Fig. S6 Thermal dependence of the strains from *HSls* state quenched at 30 K. The thermal relaxation from the *HSls* state quenched at 30 K to the *LShs* phase occurs around 65 K, as characterized by the thermal evolution of the volume strain v_s and the ferroelastic strain ϵ_{13} in the *HSls* (red) and *LShs* (blue) phases.

Supplementary Section 4: Symmetry-breaking Bragg peaks.

The symmetry-breaking from the $Pccn$ $LShs$ space group to the $P2_1/c$ $HSlS$ space group is also characterized by the change of Bragg peaks extinction rules. In the $Pccn$ space group, the intensities I_{hkl} of Bragg peaks indexed $0kl$ with $l = 2n + 1$, $h0l$ with $l = 2n + 1$ and $hk0$ with $h + k = 2n + 1$ are zero. In the $P2_1/c$ space group with same b axis as in the $Pccn$ space group, the intensities I_{hkl} of Bragg peaks indexed $0kl$ with $l = 2n + 1$ and $hk0$ with $h + k = 2n + 1$ are not restricted to zero anymore. The corresponding Bragg peaks with intensity $I_{hkl} \propto \eta^2$ are highlighted in Fig. S7.

For example, in the space group $Pccn$, the c glide plane $\perp a$ relates atomic coordinates:

$$(x_j, y_j, z_j) \rightleftharpoons (-x_j, y_j, z_j + \frac{1}{2}).$$

The structure factor of $0kl$ Bragg splits into two contributions from these equivalent atoms:

$$F_{0kl} = \sum_j f_j \left[e^{(2i\pi(ky_j + lz_j))} + e^{(2i\pi(ky_j + l(z_j + \frac{1}{2})))} \right] = \sum_j f_j \left[e^{(2i\pi(ky_j + lz_j))} \right] [1 + (-1)^l]$$

Therefore, if there is a c glide plane $\perp a$ $F_{0kl} = 0$ for $l = 2n + 1$ and the intensity $I_{0kl} = 0$.

Due to symmetry-breaking with amplitude η and loss of this glide plane, there is a relative shift of initially equivalent atoms by $\Delta z_j \propto \eta$: $(x_j, y_j, z_j) \rightleftharpoons (-x_j, y_j, z_j + \Delta z_j + \frac{1}{2})$

$$F_{0kl} = \sum_j f_j \left[e^{(2i\pi(ky_j + lz_j))} + e^{(2i\pi(ky_j + l(z_j + \Delta z_j + \frac{1}{2})))} \right] = \sum_j f_j \left[e^{(2i\pi(ky_j + lz_j))} \right] [1 + (-1)^l e^{(2i\pi l \Delta z_j)}]$$

$$F_{0kl} = \sum_j f_j \left[e^{(2i\pi(ky_j + lz_j))} \right] [1 + (-1)^l (1 + 2i\pi l \Delta z_j)] \propto \eta \text{ for } l = 2n + 1$$

Therefore, the intensity of the symmetry-breaking Bragg peaks $I_{hkl} \propto \eta^2$.

The X-ray diffraction data show that the after synthesis at room temperature the ferroelastic high temperature phase corresponds to a single domain.

LShs (*Pccn*)

HSIs (*P2₁/c*)

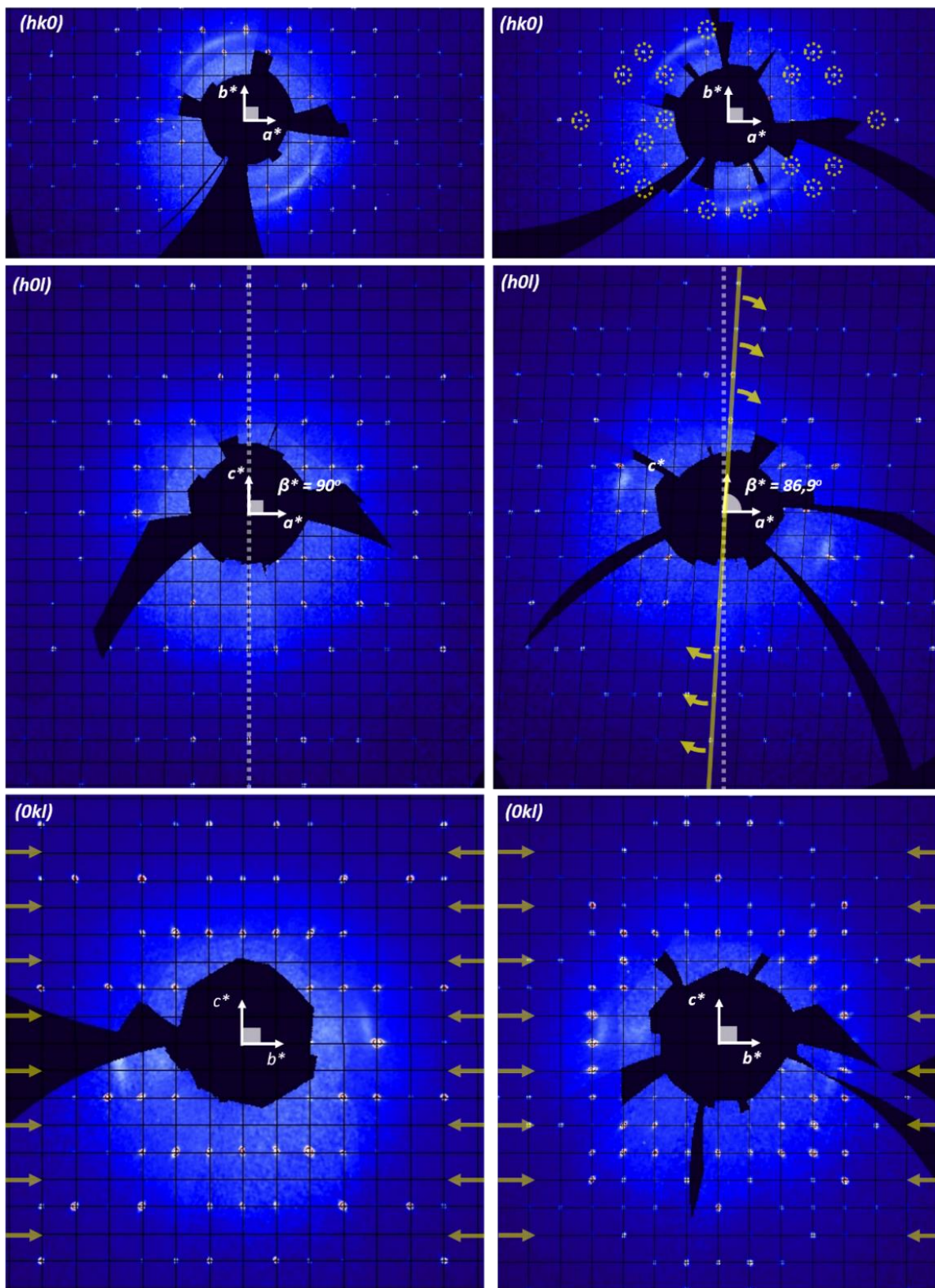


Fig. S7 Symmetry-breaking in the reciprocal space. **a**, diffracted intensity in the $(hk0)$ plane showing that the extinction at the nodes of the reciprocal space indexed $h + k = 2n + 1$ in the *LShs Pccn* phase is suppressed in the *HSIs P2₁/c* phase as indicated by yellow dotted circumferences. **b**, diffracted intensity in the $(h0l)$ plane showing the distortion of the reciprocal lattice where β^* deviates from 90° in the *LShs Pccn* phase to 86.9° in the *HSIs P2₁/c* phase. **c**, diffracted intensity in the $(0kl)$ plane showing that the extinction in the rows $l = 2n + 1$ marked by arrows in the *LS Pccn* phase is suppressed in the *HS P2₁/c* phase.

Supplementary Section 5: DFT calculations.

DFT geometry optimizations were carried out by using the Gaussian 16 (revision A.03) package¹⁰ with the PBE0 hybrid functional^{11, 12} and tightening both self-consistent field (10^{-10} au) and geometry optimization (10^{-5} au) convergence thresholds. The “Stuttgart/Dresden” basis sets and effective core potentials were used to describe the iron atom,¹³ whereas all other atoms were described with the SVP basis sets.¹⁴

We performed DFT calculations on the isolated molecule in the *LShs* and *HShs* states with optimized molecular structure with C2 symmetry and in the *HSls* state with C1 symmetry. The energy diagram of t_{2g} -like and e_g -like orbitals in C2 symmetry (*LShs* and *HShs*) shows two pairs of degenerate orbitals: $d(y^2) - d(2y^2 - x^2 - z^2)$ like and $d(xy) - d(yz)$ like, labelled as such since the 2-fold symmetry axis is along the y direction. These orbitals highlight that the two NCS groups and the two PM-PEA ligands are symmetry-equivalent with respect to the 2-fold axis. The C2 structure of the *HShs* state is unstable, as a low symmetry torsion mode Q_T (B symmetry) exhibits a negative frequency. The atomic motions of this torsion mode, shown in Fig. S8, break C2 symmetry with a displacement of the Fe out of the 2-fold symmetry axis. The associated torsions of the NCS groups are similar to the torsions observed in the *HSls* crystalline structure. The mode is shown in supplementary movie 1. In the C1 *HSls* state, the degeneracy is lifted and orbitals are asymmetric, especially around the NCS groups (Fig. S8). Both the motion of the NCS groups along the unstable Q_T mode in *HShs* state and asymmetric spin density on the NCS groups in the *HSls* state (Fig. S9), explain the coupled changes of spin state and symmetry and the different torsions of the NCS groups observed in the crystalline structure of the *HSls* state. The structural parameters around the FeN₆ coordination sphere are given in Table S2, where we can see a nice global agreement between DFT and XRD results, considering that DFT calculations are performed on an isolated molecule. The difference between DFT calculations and XRD measurements is very likely due to the molecular packing in the crystal.

Based on the calculated vibration modes λ for *HSls* and *LShs* states (Table S3), we calculate the vibrational entropy difference, due to frequency changes from ν_λ^{LShs} to ν_λ^{HSls} . The usual low frequency approximation^{15, 16} with dominant contribution of 47 modes below 400 cm^{-1} gives

$$\Delta S_{vib} = R \sum_\lambda \ln\left(\frac{\nu_\lambda^{LS}}{\nu_\lambda^{HS}}\right) = 58.3 \text{ J.K}^{-1}.\text{mol}^{-1}.$$

Including the contribution of the 3 acoustic modes, considering a global softening scaling with the speed of sound ratio of the order of 1.1 between LS and HS states, gives a global vibrational entropy contribution $\Delta S_{vib} = 58.9 \text{ J.K}^{-1}.\text{mol}^{-1}$.

This large vibrational entropy increase from *LShs* to *HSls* is mainly due to the change of spin state. Indeed, the frequencies of the modes of the *HShs* and *HSls* states, are very similar, except for the unstable low symmetry torsion mode Q_T discussed above.

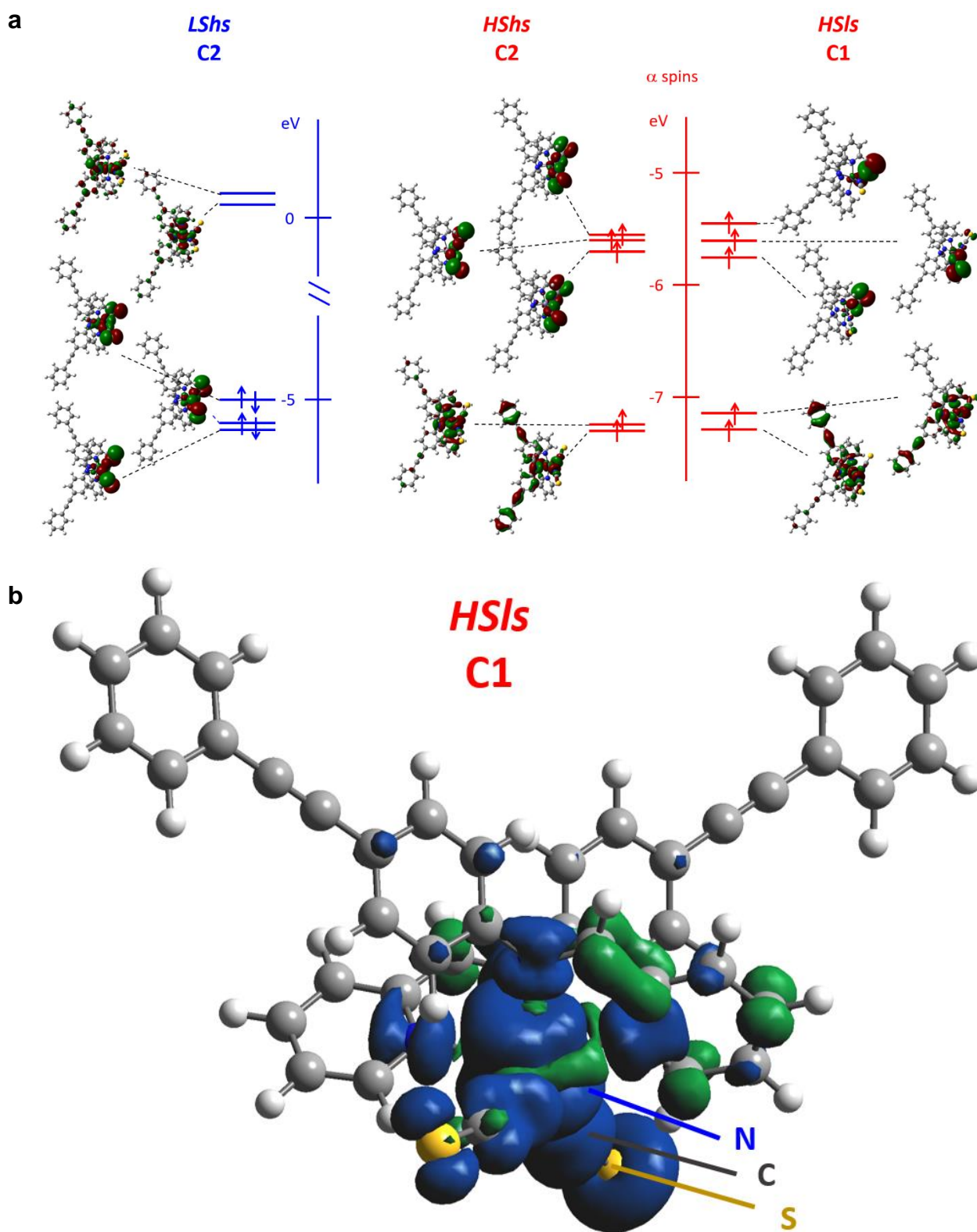


Fig. S8. Orbital energy diagram. **a**, optimized and stable molecular structures for the C2 *LShs*, C2 *HShs* and C1 *HSIs* states. Only α spins are shown for clarity. **b**, α spin density for one orbital in the C1 *HSIs* state showing different densities around the NCS groups equivalent in C2 symmetry.

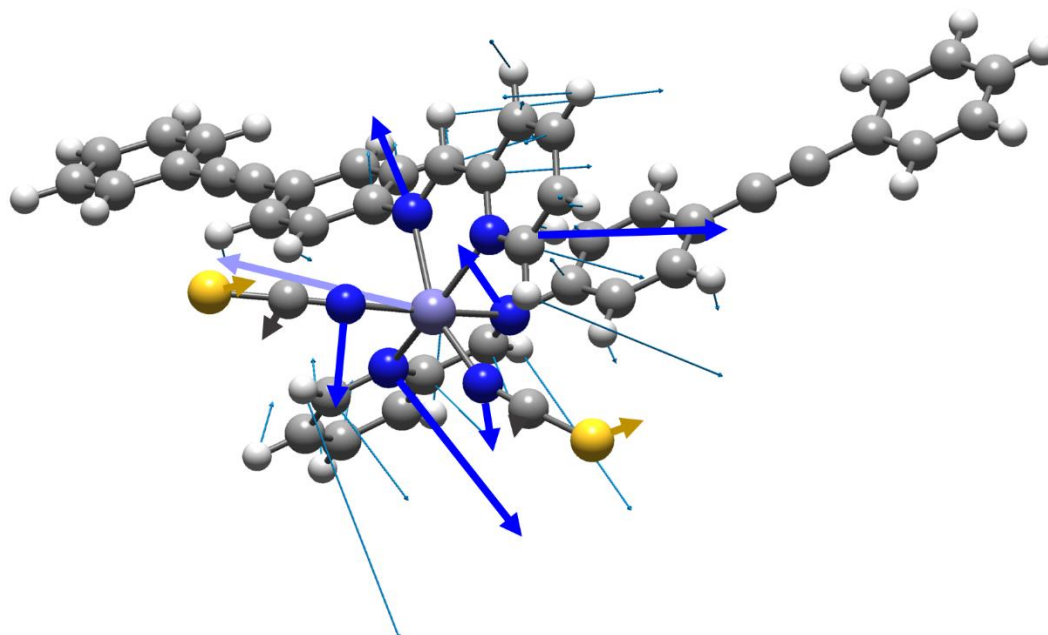


Fig. S9. Unstable mode in the *HShs* state. The optimized molecular structure in *HShs* state with C2 symmetry exhibits one vibrational mode with negative frequency. It corresponds to a torsion low symmetry torsion mode Q_T (B symmetry). The relaxation along this mode brings the system to the stable *HSlS* state. The motions of the Fe, N and NCS groups are highlighted for clarity.

Table S3. Vibrational modes frequencies. For *HSlS* and *LShs* states (below 400 cm^{-1}).

Mode n°	ν_{HSlS} (cm^{-1})	ν_{LShs} (cm^{-1})	Mode n°	ν_{HSlS} (cm^{-1})	ν_{LShs} (cm^{-1})	Mode n°	ν_{HSlS} (cm^{-1})	ν_{LShs} (cm^{-1})
1	5.62	8.69	18	63.69	70.37	35	187.05	232.30
2	10.41	10.93	19	69.14	73.50	36	189.88	243.46
3	11.50	12.53	20	79.84	103.86	37	212.06	268.12
4	16.10	14.57	21	82.99	109.62	38	246.74	275.83
5	16.45	14.84	22	99.11	117.45	39	251.25	310.58
6	17.39	20.23	23	101.18	119.15	40	280.49	313.02
7	20.52	21.26	24	116.00	138.32	41	292.60	322.68
8	21.76	22.01	25	127.99	144.01	42	302.39	334.86
9	23.60	31.49	26	130.32	151.47	43	304.69	346.09
10	26.05	34.28	27	139.65	176.69	44	313.57	355.47
11	29.23	37.42	28	142.20	186.48	45	314.70	365.99
12	34.69	38.29	29	142.46	192.24	46	348.65	387.09
13	39.25	41.20	30	151.17	200.87	47	349.57	395.21
14	45.00	43.94	31	165.90	209.90			
15	53.32	50.21	32	168.12	211.21			
16	58.43	62.41	33	178.02	216.79			
17	62.57	69.79	34	183.41	224.75			

Supplementary Section 6: Landau model of coupled symmetry-breaking and SCO.

6.a Lowest order Landau potential

Here we introduce a simpler version of the Landau potential to describe the coupled SC and SB,¹⁷⁻¹⁹ through a Taylor development of the SB (η) and SC (q) order parameters. q corresponds to an isosymmetric transformation, without restriction of orders in the development. Due to the loss of the C2 axis, the thermodynamic potential should satisfy the $G(\eta) = G(-\eta)$ relationship and therefore only even orders of η are allowed.³ As starting point we use the lowest order and relevant Gibbs potential, whose solutions can be derived analytically:

$$G(q, \eta) = Aq + \frac{B}{2}q^2 + \frac{b}{4}\eta^4 + Dq\eta^2 \quad (5.1)$$

The q, q^2 terms describe the spin conversion potential, with $B > 0$ for stability and $A = a_I(T_{SC} - T)$ is the reduced temperature. For limiting the number of parameters, we consider hereafter B, b and D constant. The symmetry-breaking terms include η^4 , with $b > 0$ for stability and the coupling term $D < 0$ for stabilizing the *LShs* and *HSlS* phases. In order to find the stable solutions for η in equation (4), we use the stability conditions:

$$\frac{dG}{d\eta} = 0 = (\eta^2 + 2Dq)\eta \quad \text{and} \quad \frac{d^2G}{d\eta^2} > 0, \quad \text{which gives two solutions:}$$

- $\eta = 0$, restricting $2Dq > 0$, corresponds to *LShs* phase ($q < 0, \eta = 0$)
- $\eta = \pm \sqrt{-\frac{2Dq}{b}}$, restricting $\eta^2 > -\frac{2Dq}{3b}, q > 0$, for the *HSlS* phase ($q > 0, \eta \neq 0$)

By substituting both solutions for η into equation (5.1), two expressions for the thermodynamic potential are obtained, corresponding to the *LShs* (5.2) and *HSlS* (5.3) phases: 0

$$- \quad G_{LShs} = G(q, \eta = 0) = Aq + \frac{B}{2}q^2 \quad (5.2)$$

$$- \quad G_{HSlS} = G(q, \eta \neq 0) = Aq + \left(\frac{B}{2} - \frac{D^2}{b}\right)q^2 \quad (5.3)$$

It is then straightforward to describe the thermal evolution of the equilibrium value of q , considering the spin transition parameter as explicitly restricted to $-1 \leq q \leq 1$. The stability limits with temperature of *HS* and *LS* states can be analytically found with:

$$\left. \begin{aligned} \frac{dG(q, \eta = 0)}{dq} \Big|_{q=-1} &= 0 \\ q &= \frac{-a_0(T_{SC} - T)}{B} \Big|_{q=-1} \\ T_1 &= \frac{-B}{a_0} + T_{SC} \end{aligned} \right| \quad \left. \begin{aligned} \frac{dG(q, \eta^2 = -\frac{2Dq}{b})}{dq} \Big|_{q=1} &= 0 \\ T_2 &= \frac{2}{a_0} \left(\frac{B}{2} - \frac{D^2}{b} \right) + T_{SC} \end{aligned} \right.$$

The thermal evolution of the potential along q and the thermal dependence of equilibrium q and η are shown in Fig. S10. Below T_1 q is restricted to -1 and in the *LS* phase it linearly increases between T_1 and T_{SC} , where $q = 0$ is the stability limit.

This *LS* phase stable below T_{SC} is high symmetry (*LS*hs, $q > 0$, $\eta = 0$). Above T_{SC} , the strong coupling D stabilizes the *HS* phase with q fixed to 1 and $\eta = \sqrt{-\frac{2D}{b}}$. On cooling, this *HS* phase is stable down to T_2 , where the phase transition towards the *LS*hs phase occurs.

The hysteresis width, $T_{SC} - T_2 = -\frac{2}{a_0}(\frac{B}{2} - \frac{D^2}{b})$, is enlarged by the coupling D , which is also responsible for the appearance of an energy barrier in the *HS* state (Fig. S10), precluding relaxation towards the *LS* state. This lowest order Gibbs potential has the advantage to provide analytical solutions reproducing the stepwise evolution of the symmetry-breaking order parameter η and the unsymmetric hysteresis loop of the spin transition order parameter q .

However, the Taylor development limited to q^2 gives a linear evolution of q on warming. In the main text, we add a q^4 term in the potential in equation (1). The solutions are no more analytical and equilibrium q is found numerically. Fig. 4 shows that this potential provides a gradual thermal conversion on warming from the *LS* state and reproduces very well experimental data, catching so the main physical parameters behind the physics of coupled symmetry-breaking and spin crossover.

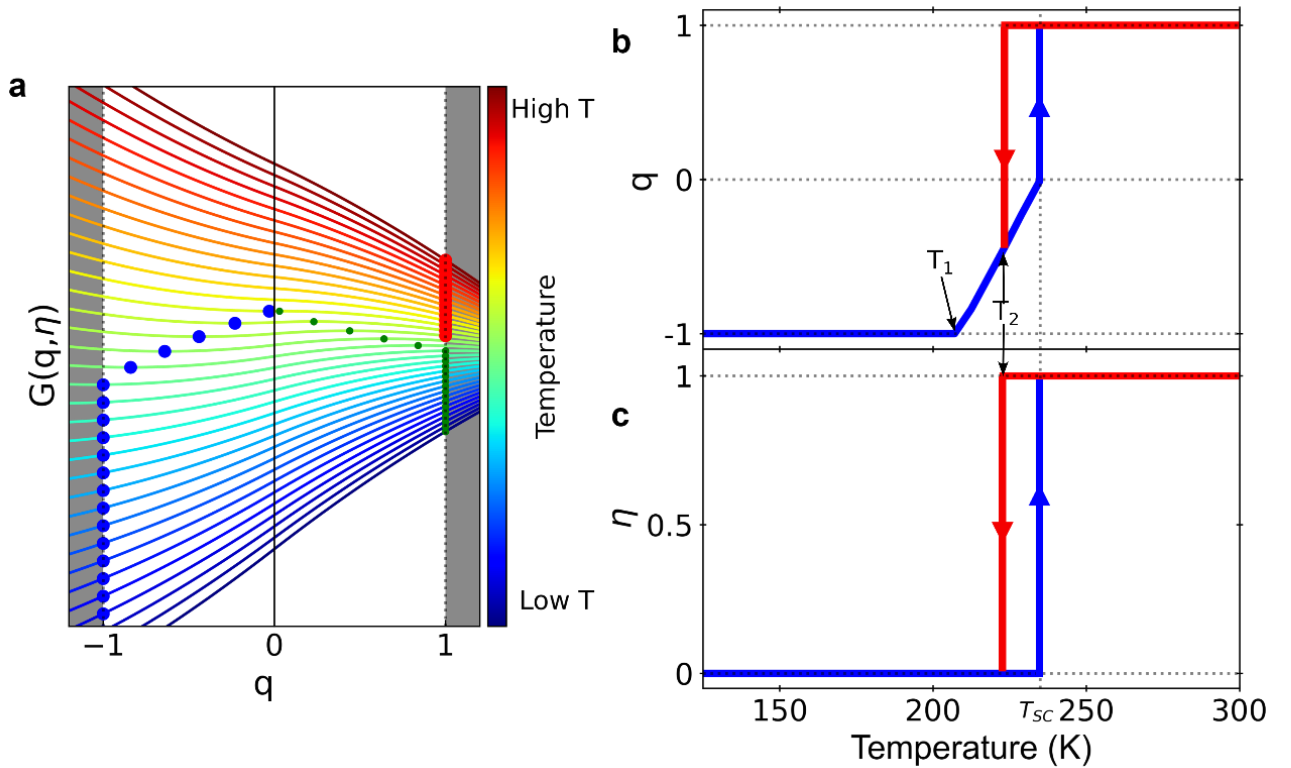


Fig. S10 Lowest order Landau Model. **a**, Thermal dependence the Gibbs potential along the spin crossover parameter q . These minima are represented by blue and red dots for *LS* and *HS* states, respectively, while the maxima in the *HS* region (height of energy barrier) is marked with green dots. The minima correspond to the thermal equilibrium of q (**b**) and η (**c**). Results obtained from Eq (5.1) with $a_1 = 0.3$, $B = 8$, $b = 2$, $T_{SC} = 235$ K, $D = -4$.

6.b Higher order Landau potential

In the manuscript we consider the Landau potential:

$$G(q, \eta) = a_1(T_{SC} - T)q + \frac{B}{2}q^2 + \frac{C}{4}q^4 + \frac{a_0}{2}(T - T_c)\eta^2 + \frac{b}{2}\eta^4 + Dq\eta^2 + \frac{E}{2}q^2\eta^2 \quad (5.4)$$

and discussed the strong coupling limit, for which $(\frac{a_0}{2}(T - T_c) \ll Dq)$. The theoretical results are then matching very well the experimental data in the vicinity of the $LShs \rightarrow HSls$ phase transition. However, in this strong coupling limit, the symmetry-breaking order parameter is found to be constant in the HT phase ($\eta = \sqrt{-(2Dq + E q^2)/b}$, were q is fixed to 1. This does not fit with experimental data at much higher temperature. Indeed, the X-ray diffraction data in Fig. S5 shows that $\varepsilon_{13} \propto \eta$ decreases at much higher temperature, and is extrapolated to vanish around 800 K. This indicates the presence of a hypothetical and hidden high spin phase with high symmetry ($Pccn$) at much higher temperature. This can be explained by considering the influence of the $\frac{a_0}{2}(T - T_c)\eta^2$ term in the Landau model. In this case, a high spin high symmetry phase ($HShs$, $q=1$, $\eta=0$) is found to be stable above the temperature $T_{SB} = (T_c - \frac{2D}{a_1} - \frac{E}{a_1})$.

Fig. S11 shows the thermal dependence of q and η obtained from the potential in equation (5.4), which reproduces the stepwise changes of $q(T)$ and $\eta(T)$ observed on cooling in Fig. 2a and 2b and the decrease of η at higher temperature, matching so the global experimental data. This $HShs$ phase, which corresponds to the HS parent paraelastic phase, is however not observed experimentally as sample melts around 500 K.

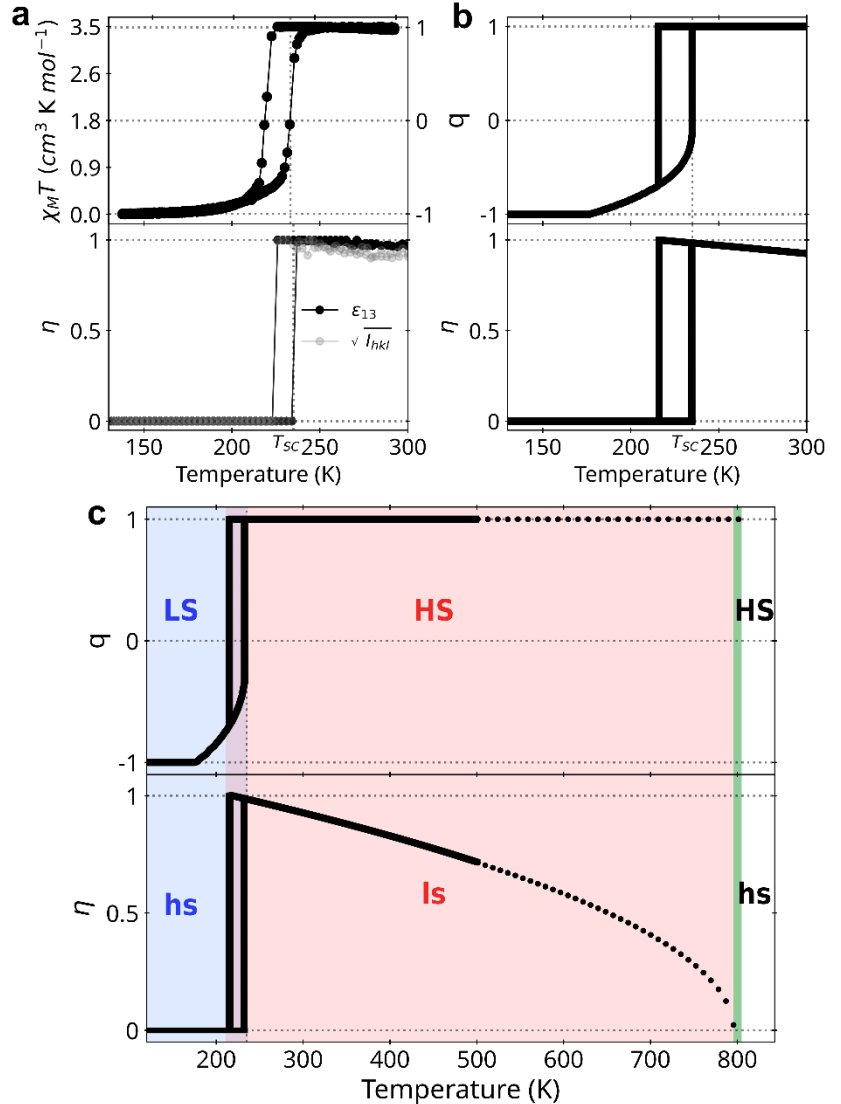


Fig. S11 Higher order potential.

Thermal dependence of the SC (q) and SB (η) parameters extracted from equation (5.4), with the stepwise and ascending $LShs \rightarrow HSls$ SB (upper panel) and the decrease of η at higher temperature, towards a hypothetical and hidden $HShs \rightarrow HShs$ phase transition around 800 K. Results obtained from Eq (5.4) with $a_0 = 0.6$, $a_1 = 0.0185$, $B = 0$, $C = 35$, $b = 10$, $T_{SC} = 235$ K, $D = -6.5$, $E = -12.2$

Supplementary Section 7: Differential scanning calorimetry measurements.

DSC measurements were performed in the 115–295 K temperature range under argon on a Perkin Elmer calorimeter DSC8000 coupled with CLN2 regulator setting the scan rate of 5 K.min⁻¹ on crystals (mass of 8.034 mg). The Cp curves are shown in shown in Fig. S12. This phase transition occurs with an enthalpy changes $\Delta H = 15.23$ kJ.mol⁻¹ and $\Delta H = 14.63$ kJ.mol⁻¹ for the heating (242.6 K) and cooling peaks (216.4 K) respectively. These data correspond to transition entropy values of $\Delta S = 62.8$ J.mol⁻¹.K⁻¹ and $\Delta S = 67.6$ J.mol⁻¹.K⁻¹. The small difference between DSC peak positions compared to X-ray and magnetic data is most likely due to a kinetic effect.

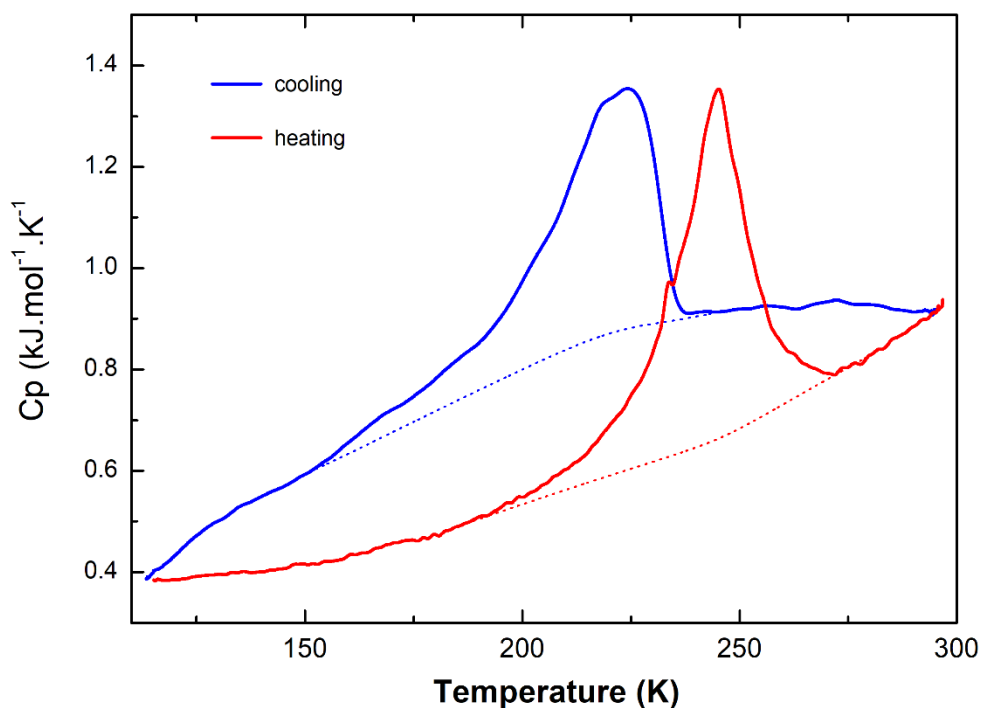


Fig. S12 Calorimetric study. Heat capacity on cooling and warming.

Supplementary references

1. E. Collet and P. Guionneau, *Cr Chim*, 2018, **21**, 1133-1151.
2. M. A. Carpenter, E. K. H. Salje and A. Graeme-Barber, *Eur. J. Mineral.*, 1998, **10**, 621-691.
3. E. K. H. Salje, *Annual Review of Materials Research*, 2012, **42**, 265-283.
4. V. Janovec, V. Dvořák and J. Petzelt, *Czechoslovak Journal of Physics B*, 1975, **25**, 1362-1396.
5. P. Guionneau, F. Le Gac, S. Lakhoufi, A. Kaiba, D. Chasseau, J. F. Létard, P. Négrier, D. Mondieig, J. A. K. Howard and J. M. Léger, *Journal of Physics: Condensed Matter*, 2007, **19**, 326211.
6. G. Sheldrick, *Acta Crystallographica Section A*, 2015, **71**, 3-8.
7. G. Sheldrick, *Acta Crystallographica Section C*, 2015, **71**, 3-8.
8. O. V. Dolomanov, L. J. Bourhis, R. J. Gildea, J. A. K. Howard and H. Puschmann, *Journal of Applied Crystallography*, 2009, **42**, 339-341.
9. J. Rodríguez-Carvajal, *Physica B: Condensed Matter*, 1993, **192**, 55-69.
10. M. J. e. a. Frisch, *Gaussian, Inc., Wallingford CT*, 2016.
11. J. P. Perdew, K. Burke and M. Ernzerhof, *Physical Review Letters*, 1996, **77**, 3865-3868.
12. C. Adamo and V. Barone, *The Journal of Chemical Physics*, 1999, **110**, 6158-6170.
13. M. Dolg, U. Wedig, H. Stoll and H. Preuss, *Journal of Chemical Physics*, 1987, **86**, 866-872.
14. F. Weigend and R. Ahlrichs, *Physical Chemistry Chemical Physics*, 2005, **7**, 3297-3305.
15. G. Privault, J.-Y. Mevellec, M. Lorenc, B. Humbert, E. Janod, N. Daro, G. Chastanet, A. Subedi and E. Collet, *Cryst Growth Des*, 2022, **22**, 5100-5109.
16. G. Molnár, M. Mikolasek, K. Ridier, A. Fahs, W. Nicolazzi and A. Bousseksou, *Ann Phys-Berlin*, 2019, **531**, 1900076.
17. E. Collet, G. Azzolina, J. Jeftić and M.-H. Lemée-Cailleau, *Advances in Physics: X*, 2023, **8**, 2161936.
18. G. Azzolina, R. Bertoni and E. Collet, *Journal of Applied Physics*, 2021, **129**, 085106.
19. E. Collet and G. Azzolina, *Physical Review Materials*, 2021, **5**, 044401.